metals

MDPI

Article

Monte-Carlo-Assisted Phase Field Simulations of Grain Structure Evolution during the Welding Process

Ying Zheng [1,2], Jiangping Liu [2], Yongfeng Liang [3] and Pingping Wu [1,2,4,*]

[1] Department of Materials Science and Engineering, Xiamen Institute of Technology, Xiamen 361021, China
[2] The Higher Educational Key Laboratory for Flexible Manufacturing Equipment Integration of Fujian Province, Xiamen Institute of Technology, Xiamen 361021, China
[3] State Key Laboratory for Advanced Metals and Materials, University of Science and Technology Beijing, Beijing 100083, China; liangyf@skl.ustb.edu.cn
[4] State Key Laboratory for Mechanical Behavior of Materials, Xi'an Jiaotong University, Xi'an 710049, China
* Correspondence: pingpingwu@xit.edu.cn

Abstract: A Monte-Carlo-assisted phase field model for the simulation of grain growth in metals and alloys is presented. The simulation time in this model is connected to real time through an experimental data-based kinetic model. Site selection probability is introduced to simulate grain structure evolution under non-isothermal conditions. The grain evolutions with temporal and spatial distributions of temperature during the welding process are comprehensively reproduced. The average size and topological texture of the generated grains in the fusion zone and heat-affected zone are examined. The computed results are compared to experimental data for laser-welding two alloys: Fe–6.5 wt.%Si and low-carbon steel. The applications of real-time–temperature based phase field simulation to material processing indicate significant promise for understanding grain structures during the welding process or additive manufacturing processes.

Keywords: grain structures; phase field model; Monte Carlo technique; welding process

Citation: Zheng, Y.; Liu, J.; Liang, Y.; Wu, P. Monte-Carlo-Assisted Phase Field Simulations of Grain Structure Evolution during the Welding Process. *Metals* **2023**, *13*, 623. https://doi.org/10.3390/met13030623

Academic Editor: Alain Pasturel

Received: 9 February 2023
Revised: 14 March 2023
Accepted: 17 March 2023
Published: 20 March 2023

1. Introduction

The grain structure and its evolution are rather important for material properties in welding and additive manufacturing processes [1]. Not only are the mechanical properties of a material critically related to its grain structure but also the accumulation of residual stress during welding and additive manufacturing can lead to the failure of the material [2,3]. Both additive manufacturing and welding processes have a fusion zone of liquid metal, under the effect of high temperature, a non-melted heat-affected zone (HAZ) formed between the melted metal and the unaffected base metal. Considering the influence of significant temperature gradients, the grain size in the HAZ is uniformly distributed due to the rate of grain boundary migration being proportional to the temperature. For a moving heat source, the geometry of the fusion zone and the HAZ changes with time, and the topological shape of the grain and grain distributions are strongly influenced by welding speeds and the temperature of the heat source; therefore, a special grain distribution pattern is generated. As many physical properties, including mechanical, thermal, and electromagnetic properties, at joints are linked to the final grain structures developed in the welding process, it is particularly important to study the grain growth process in the HAZ and the fusion zone during the welding process.

The prediction of the evolution of grain structures during the welding process has attracted great interest in the context of robotics welding applications. As a mesoscopic scale calculation method, the phase field model is ideally suited to study the grain structures of materials [4,5]. Since this method avoids tracing interfaces and the simulated structure generated is comparable to the experimental results, phase field methods have been widely used in predicting grain growth under various solidification and diffusion conditions for

over 20 years [4–14]. The phase field method simulates the microstructure evolution based on the thermodynamics and kinetics of materials with physically informed parameters. These material parameters or coefficients can be provided by first-principle calculations or directly measured with experimental data.

Recently, phase field simulation was used in the calculation of grain distributions under welding conditions [15–24]. Prosgolitis et al. [17] and Yang et al. [18] used a multi-phase field model to study the dynamical recrystallization process during the friction stir welding process. Zheng et al. [19], Wang et al. [20], and Yu et al. [21] investigated the dendrite grain growth process in a welding molten pool for Al–Cu alloy; however, almost all their works were based on the directional solidification phase field model, and the orientations in each grain were not predicted. Knowing the orientation of the grains during the welding process and how grain orientation affects the mechanical properties of materials is an essential part of creating strong and lasting welds. Little work has been performed to simulate the final grain pattern in the fusion zone (FZ) and the heat-affected zone (HAZ) considering a 3D temperature gradient.

Monte Carlo techniques based on probability theory are widely used to simulate the grain growth process in the heat treatment and welding process [25–31]. An experimental data-based (EDB) Monte Carlo grain growth model developed by Gao et al. [26] can effectively connect the simulation time and real time, taking into account the effect of the temperature of materials. Therefore, the EDB model was adopted to simulate the grain structure under isothermal conditions and heating/cooling treatment. Radhakrishnan et al [25]. and Sista et al. [28] introduced "site selection probabilities" to control the rate of grain boundary migration and simulate grain structures under non-isothermal conditions. Recently, this method was used to simulate the evolution of the grain structure and topology in 3D, considering the motion of the liquid pool for continuous linear welding [30,31]. These simulated grain structures and average grain size distribution demonstrate good agreement with actual weld microstructures. We believe that these techniques can also be applied to other mesoscopic-scale simulation methods, such as the phase field method and the cellular automata method.

In this paper, the grain growth process was simulated using a multi-phase field model assisted by Monte Carlo techniques. The simulation time was connected to real time with the EDB model proposed by Gao et al. [26]. The temporal evolution of grain structures and grain size under isothermal conditions and continuous heating treatment process were investigated and compared to independent experimental results. A 3D simulation model that took into account the temperature gradient was developed for the grain growth process under a welding condition. The size and topological structure of the generated grains in the fusion zone and the HAZ were investigated in detail. The evolution of grain structures during the welding process of Fe–6.5 wt.%Si and low-carbon steel were examined to validate the phase field simulation results with experimental data. This model can describe the temporal evolution as well as the spatial distribution of the grain structure, and it provides valuable insights into understanding the mechanism of the evolution of the grain topology during the welding process.

2. Methods

In this work, the phase field simulation code was programmed using the open source language Octave. To simulate the multi-grain structure in the phase field method, a set of order parameters η_i were chosen to identify different grains, where i represents the i^{th} grain. In the microscopic view, the orientations of grains should be connected to the order parameters η_i [5] ($i = 1, 2, 3 \ldots m$, where m is the number of orientations). Inside the i^{th} grain, $\eta_i = 1$, and outside the i^{th}-orientated grain, $\eta_i = 0$; therefore, the phase interface is the grain boundary in the multi-phase field model. Here, the time-dependent Ginzburg–Landau (TDGL) equation was chosen as the field kinetic equation in the phase field method:

$$\frac{d\eta_i(r,t)}{dt} = -L\frac{\delta F_{tot}}{\delta \eta_i(r)}, \quad (1)$$

where r is the cartesian coordinate, t is the time, L is the kinetic coefficient, and F_{tot} is the total free energy of the system. For simplicity, in our model, the total free energy includes Landau-typed chemical bulk energy F_{chem} and interfacial energy F_{inter}, i.e.,

$$F_{tot} = F_{chem} + F_{inter} \,. \tag{2}$$

Note that if one would like to simulate the mechanical properties of materials, the elastic energy term should be taken into consideration. The detailed expressions of energy terms are

$$F_{chem} = \sum_{i=1}^{m} \left(\frac{(T - T_c)}{2} {\eta_i}^2 + \frac{1}{4} {\eta_i}^4 \right) + \sum_{i=1}^{m} \sum_{j \neq i}^{m} \eta_i \eta_j, \tag{3}$$

$$F_{inter} = \sum_{i=1}^{m} \frac{\kappa}{2} (\nabla \eta_i(r))^2, \tag{4}$$

where T and T_c are the environmental temperature and the phase transition temperature, respectively. κ is the interfacial energy coefficient. The chemical energy and interfacial energy for each orientated grain are calculated, then the total free energy of the system can be obtained by summing up the energy of each grain. To improve computational efficiency, the semi-implicit Fourier spectrum method was used to solve the TDGL Equation (1).

To relate simulation time to real time, let's review the experimental empirical results first. Beck et al. [32] first suggested the following kinetic process of grain growth:

$$D = Ct^n \,, \tag{5}$$

where D is the grain size, C is a constant, and t is time. Later, Burke and Turnbull [33] deduced the following parabolic form for the isothermal grain growth process:

$$D^2 - D_0^2 = Kexp\left(-\frac{Q}{RT} \right) t \,, \tag{6}$$

where D_0 is the initial grain size and K is called the pre-exponential constant. Q is the activation energy for grain growth, R is the gas constant, and T is the temperature. This equation considers the effect of temperature on the grain growth process.

Gao et al. [26] developed an experimental data-based (EDB) model to relate simulation time to real time. In simulations, an empirical relation between the simulated grain size and simulation time t_s is suggested as

$$D = K_1 \lambda {t_s}^{n_1} \,, \tag{7}$$

where K_1 and n_1 are model constants and λ is the grid spacing. According to the EDB model, by substituting Equation (7) in Equation (6), a relationship between simulation time and real time is obtained:

$$(t_s)^{2n_1} = \left(\frac{D_0}{K_1 \lambda} \right)^2 + \frac{K}{(K_1 \lambda)^2} exp\left(-\frac{Q}{RT} \right) t \,, \tag{8}$$

It should be noted that the pre-exponential constant K and the activation energy Q for grain growth come from experimental measurements. This would allow us to simulate grain structures for different metals.

In the welding process, the temperature is a continuous function of the spatial position,

$$T = T_0 + \frac{q}{2\pi k_s d} exp\left(-\frac{v(d - x)}{2\alpha_s} \right) \,, \tag{9}$$

where T_0 is the initial temperature, q is the heat put, k_s is the thermal conductivity, d is the distance from the simulation site to the point heat source, v is the welding speed, and $\alpha_s (= k_s / \rho c)$ is the thermal conductivity, where ρc is the specific heat per unit volume.

Note that the simulation time t_s is also position dependent. To simulate the grain growth process with a temperature field $T(r)$, Sista and Debroy [28] developed a Monte Carlo scheme with a concept of "site selection probabilities" to simulate the welding temperature field. In Monte Carlo simulations, the orientation of a grain at a site has a probability to switch or not switch:

$$p(r) = \frac{t_s(r)}{t_{sMax}}, \tag{10}$$

where $t_s(r)$ is the simulation time field and t_{sMax} is the maximum simulation time. In our work, we applied this Monte Carlo algorithm in the evolution of the phase field model. The TDGL Equation (1) at a site has the probability to evolve or not evolve. The evolution probability of a site close to the fusion line is approximately equal to 100%, i.e., the order parameters are updated almost every simulation step. The higher the site probability, the more frequent the evolution of the phase field kinetic equation.

3. Application of the Model to Grain Growth and Welding Processes

The 2D phase field simulation used a matrix size of 512 × 512 grids with a periodic boundary condition. The grids were uniformly spaced, and lattice point spacing λ = 40 μm, which was assumed to be the initial base metal grain size. The number of grain orientation m was set to 10. The interfacial energy coefficient κ was set to be 2.0 to avoid the sharp interface and grid-pinning effect in simulation. The dynamic coefficient L = 1.0, and dt = 0.25. In the EDB model, the empirical parameters K_1 = 0.14 and n_1 = 0.48 [26].

3.1. Application of the Model to the Isothermal Grain Growth Process

Zone-refined tin was chosen as the aim material for simulation with the independent available experimental data [34] on isothermal grain growth kinetics. For simplicity, D_0 was set to be 0, the pre-exponential constant K = 5.17 × 10^6, Q = 6000 cal/mol, and R = 2 cal/mol/K. The final relationship between the simulation time and real time is

$$(t_s)^{0.96} = 16{,}500 \ \exp\left(-\frac{3000\ \mathrm{K}}{T}\right) t. \tag{11}$$

The simulated grain structures of zone-refined tin in an isothermal process at temperatures of 167, 185, and 220 °C are shown in Figure 1. Columns 1–4 in Figure 1 represent the simulated grain structures at 75, 150, 225, and 300 s. The calculation domain was detegrated into 512 × 512 grids, and the grid spacing was set to be 40 μm. Many millimeter-scale grains were obtained, and a significant grain growth process was observed during the isothermal process. Based on these simulation results, the computed average grain size is in good agreement with the experimental data by Holmes et al. [34], as shown in Figure 2. It should be noted that in [34], a time correction was used by the authors because the experimental time is not the true time necessary for a specimen to reach its measured grain size, and the experimental data in the form of log values were converted to normal values. In the beginning, the grain size increases rapidly, and then the growth speed decreases and the grain structure approaches a stable state. Note that the rate of grain boundary migration is inversely proportional to the average grain size. At higher temperatures, the rate of grain boundary migration increases, resulting in faster grain growth.

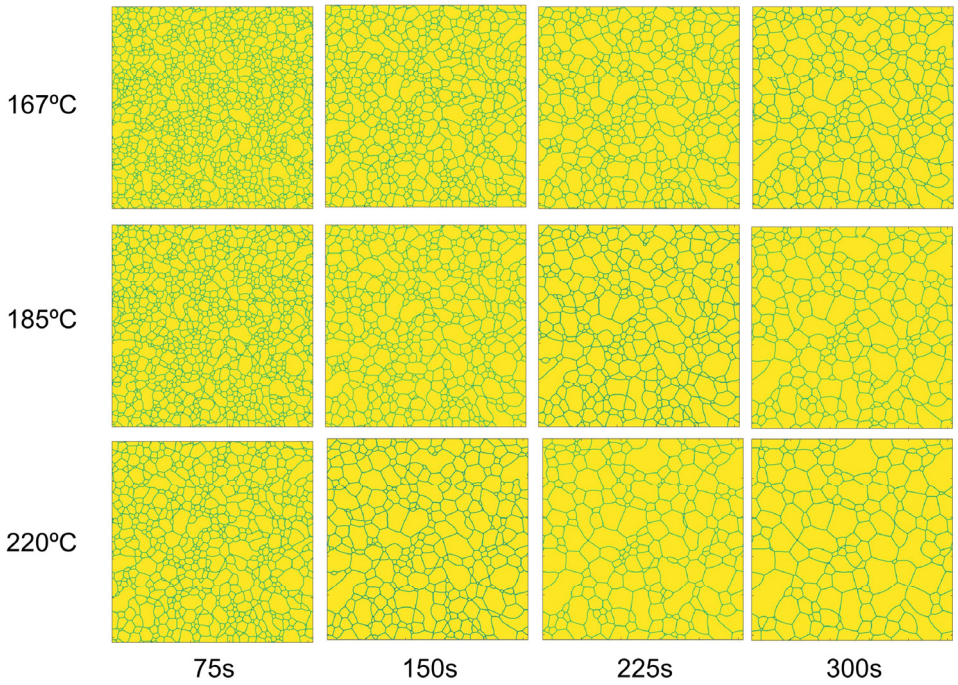

Figure 1. Simulated grain structures of zone-refined tin after 75, 150, 225, and 300 s (columns 1–4) during the isothermal process at a temperature of 167 °C, 185 °C, and 220 °C.

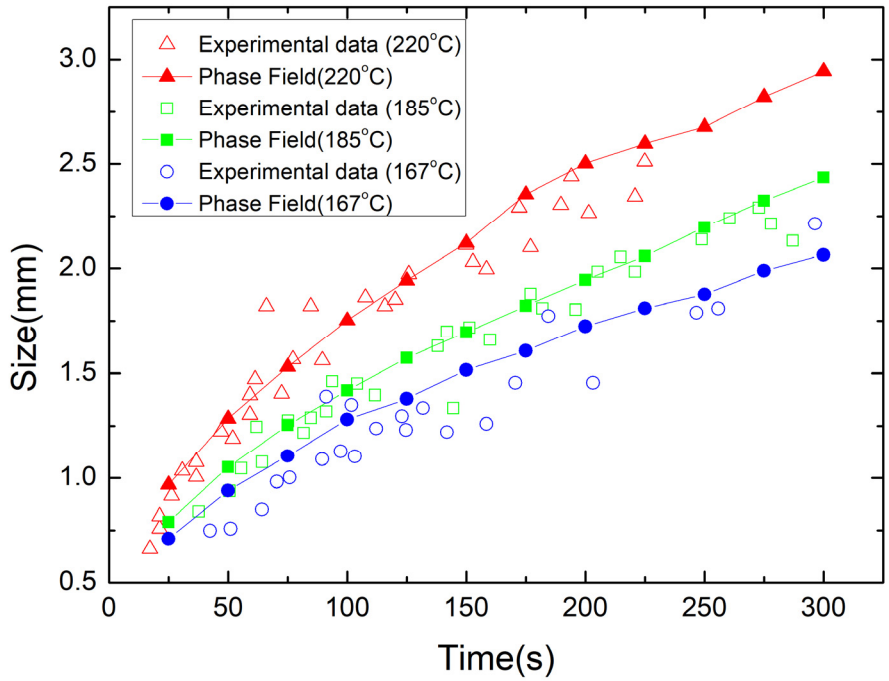

Figure 2. Comparison of simulated grain size to experimental data [34] in the isothermal grain growth process.

3.2. Application of the Model to the Continuous Heat Treatment Process

To simulate the grain growth process during the heat treatment process, first, the continuous heating process needs to be divided into a series of isothermal processes with several small time intervals. Taking a titanium alloy from Brun et al.'s experimental

work [35] as an example, the initial grain size D_0 = 3.5 μm, λ = 3.25 μm, $K = 2.02 \times 10^{12}$, Q = 251,000 J/mol, and R = 8.31/mol/K, and the simulation time t_s can be calculated by

$$(t_s)^{0.96} = \frac{625}{\lambda^2} + \frac{1.03 \times 10^{14}}{\lambda^2} \exp\left(-\frac{251,000}{RT}\right) t. \quad (12)$$

The alloy was continuously heated from 1050 °C to 1200 °C at a rate of 25 °C/s; here, we chose 1 s as a time interval and converted it into simulation steps with Equation (12). Note the number of simulation steps at different temperatures is not the same. The output simulated grain structure at the former temperature is the input grain structure in the calculation at the next temperature. Figure 3a–g shows the simulated grain structures at 1050, 1075, 1100, 1125, 1150, 1175, and 1200 °C in the heating process, respectively.

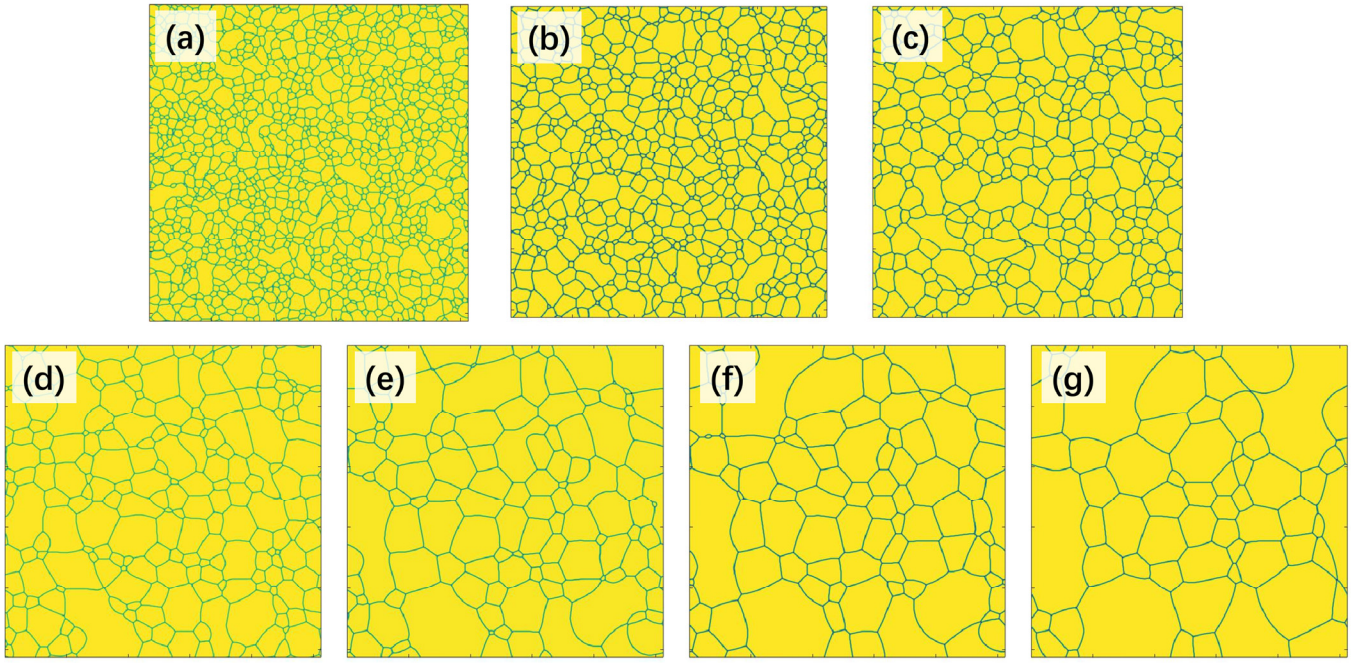

Figure 3. The evolution of grain structures during the heating process. (**a**–**g**) Simulated grain structures at 1050, 1075, 1100, 1125, 1150, 1175, and 1200 °C, respectively.

The calculated values of grain size as a function of time are plotted in Figure 4. We found that the simulation results and experimental measurements are comparable. It should be noted that the average grain size at 1050 °C is smaller than experimental data, which can be attributed to small random values used as the initial input for the phase field simulation. It is important to note that in the initial period of the simulation, the initial input grain structure is important and cannot be neglected.

3.3. Application of the Model to the Welding Process

The simulation parameters for the welding process are listed here: k_s = 26 J m^{-1}, $\rho c = 7.87 \times 10^6$ J m^{-3}, T_0 = 298 K, $q = 1.1 \times 10^3$ J s^{-1}, and $v = 1.0 \times 10^{-3}$ m s^{-1}; for Fe–Si alloy, $K = 9.38 \times 10^8$, $Q = 3.32 \times 10^5$ J mol^{-1} [36–38], and melting point T_c = 1720 K [39], and for low-carbon steel, $K = 7.38 \times 10^6$, $Q = 1.44 \times 10^5$ J mol^{-1} [40], and melting point T_c = 1811 K [39]. We used 100 × 100 × 1 discrete cells, and the initial grain size was set to be equal to grid spacing, i.e., $D_0 = \lambda$ = 40 μm.

Figure 5a illustrates the calculated temperature field in the cross-sectional plane of the weld of low-carbon steel. The liquid melted metal and solid phase were separated with a sharp interface in the current model. This sharp interface assumption was used because the grid spacing in the simulation (40 μm) is obviously greater than the solid–liquid interface thickness, which is approximately tens to hundreds of nanometers. In the liquid phase,

the temperature remains constant at the melting temperature and all the order parameters η_i were set to be 0. In the solid phase, a steep temperature gradient is created using Equation (9). In this simulation, the fusion zone was at a steady state and the dendritic substructures in grains were not considered. Figure 5b shows the distribution of the site selection probability $p(r)$ in the cross-sectional plane of the weld. Note that the probability p in the liquid phase is 0, i.e., the order parameters do not change with time and remain 0. In solid regions of higher temperature, the order parameters at the site with higher site selection probability are updated more frequently and grains grow at higher rates.

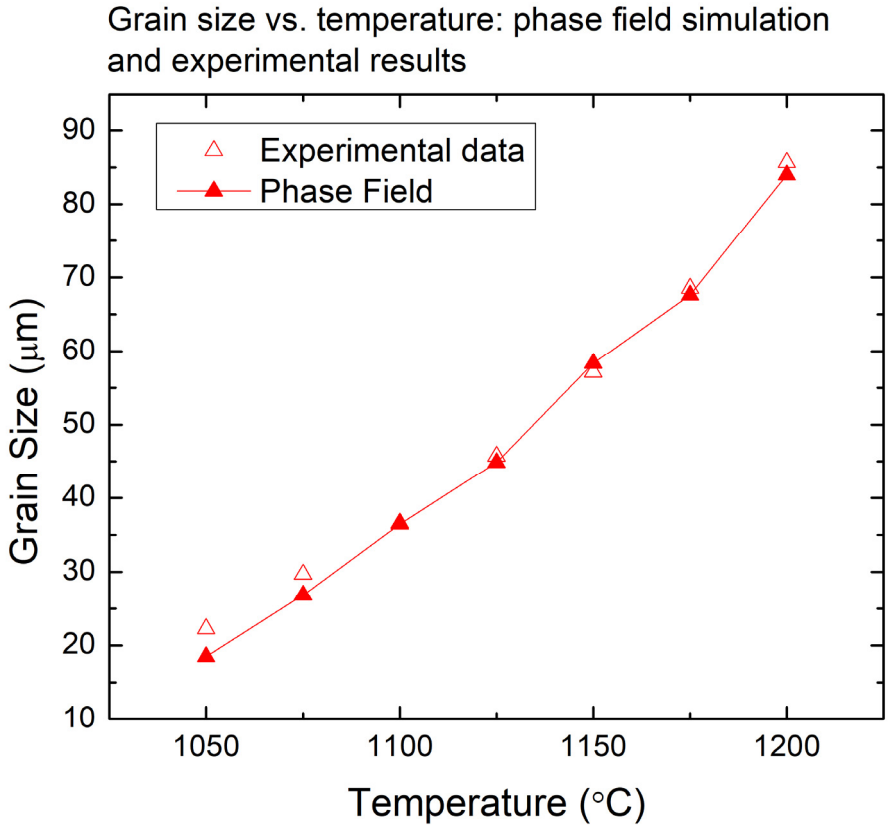

Figure 4. A comparison of the phase field calculation results of the grain size in the continuously heated alloy with the experimental data from Brun et al. [35] shows that the heating rate is 25 °C/s.

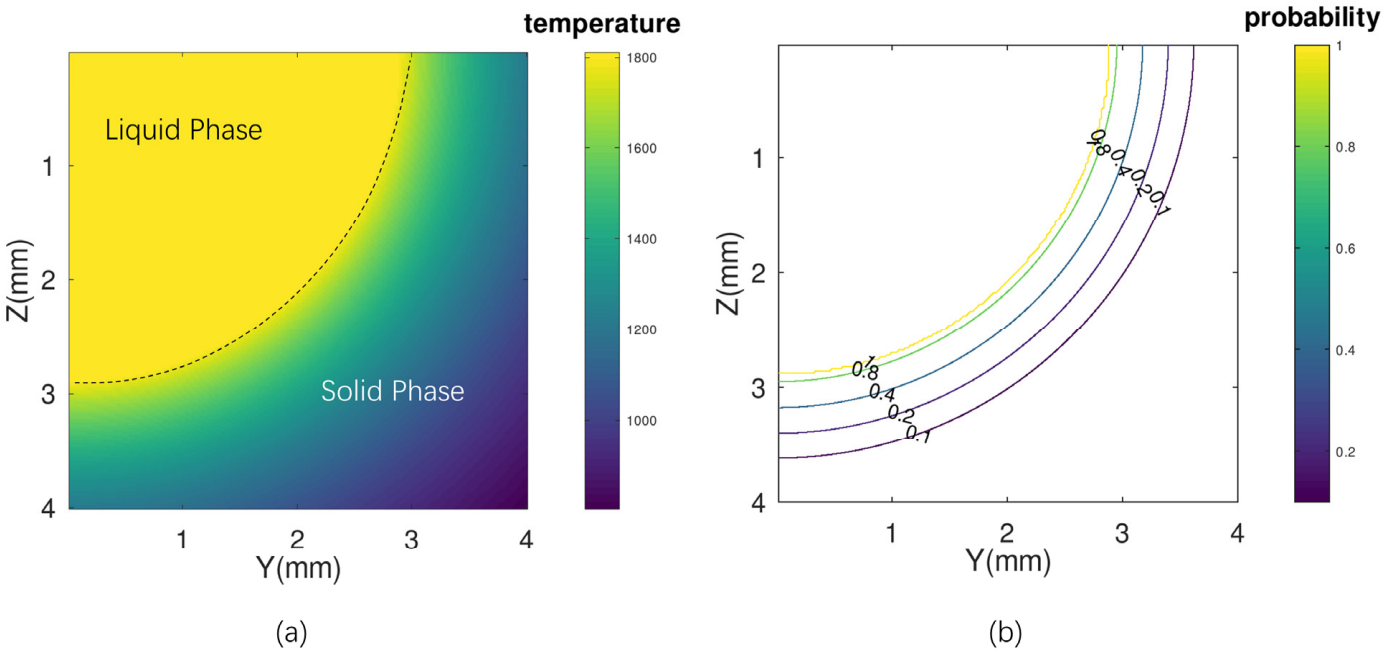

Figure 5. Computed values of (**a**) spatial distribution of temperature and (**b**) site selection probability in the cross-sectional plane of the weld of low-carbon steel.

The evolutions of the textures of grains in the HAZ of low-carbon steel and Fe–6.5 wt.% Si alloy are illustrated in Figure 6a,b. Columns 1–4 in Figure 6 represent the simulated grain structures at 100, 500, 1000, and 1500 simulation steps, respectively. For low-carbon steel, the closer the site is to the fusion zone, the higher the temperature is, leading to a higher rate of grain boundary migration, and a coarser grain size was obtained in the final grain structure. In the solid region, the grain size increases with time and is inversely proportional to the distance from the heat source. For Fe–Si alloy, the grain growth rate is larger than that in low-carbon steel. This is because the grain boundary migration is related to the thermal activation process, and in the simulation, the value of activation energy of Fe–Si alloy is much higher than that of low-carbon steel [36].

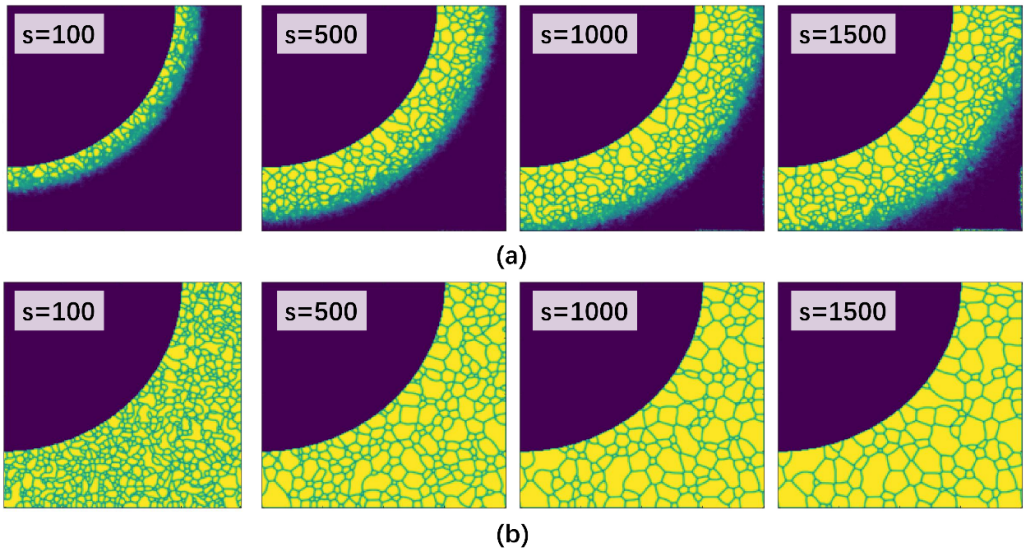

Figure 6. Computed evolution of grain structures in the HAZ of (**a**) low-carbon steel and (**b**) Fe–6.5 wt.% Si alloy in the cross section perpendicular to the direction of welding.

During the fusion welding process, as the heat source is moving, the fusion zone and the spatial distribution of temperature are time dependent; therefore, the HAZ near the fusion zone undergoes a heating and cooling process. To simulate a realistic welding process, 3D simulations are required. To reduce computer memory usage in the 3D model, we discretized the simulation cell using $120\Delta x_1 \times 80\Delta x_2 \times 40\Delta x_3$, where $\Delta x_1 = \Delta x_2 = 0.2$ mm and $\Delta x_3 = 0.1$ mm. The corresponding domain size was around 24 mm × 16 mm × 4 mm in the welding model. The scanning speed of the heat source was set to 0.1 mm/10 simulation step; the heat source moved one step ahead, and then the spatial temperature field was updated. The final structure took 1500 simulation steps, and the heat source moved 15 mm. Figure 7a shows the grain structure in the HAZ at the simulation steps of 100, 500, 1000, and 1500 during the welding process of joining two Fe–6.5 wt.% Si alloys. A similar topological texture of the grain growth process in the HAZ was observed in the 3D simulation. As a result of the heat source, equiaxed grains are generated and grow in the weld metal. Fresh solidified grains at the tail of the fusion zone grow into columnar grains as the fusion zone moves along. Under the action of the heat source, the columnar grains continue to grow in curved shapes toward the center of the fusion zone. Equiaxed grains coexist with columnar grains under welding conditions. We also observed competitive growth among grains and the vanishing of some small-size grains in the simulation.

When joining low-carbon steel to Fe–6.5 wt.% Si alloy using fusion welding, the fusion zone in the two alloys and the grain–structure evolution in the HAZ of the two alloys were different, as shown in Figure 7b. The calculation domain selected for the simulation was separated into three parts: the HAZ of low-carbon steel, the HAZ of Fe–6.5 wt.% Si alloy, and the fusion zone (which is a mixture of the former two alloys). For simplicity, the simulation parameters in the fusion zone were set as the average of the parameters of the two alloys. Columnar grains were generated and grew parallel to the top horizontal plane, which can be clearly observed in the simulations. In the fusion zone and the HAZ in the site of Si–Fe alloys, similar grain structure evolution was obtained, as seen in Figure 7b. The grains in the HAZ of low-carbon steel started growing near the fusion boundary due to the heating that occurs ahead of the fusion zone. With the movement of the fusion zone, solidification takes place and the grains grow into the reduced fusion zone area and gradually transform into columnar grains. These columnar grains continue to generally grow toward the fusion zone and are coarse and curved rather than straight shapes as the fusion zone moves along at a constant speed. In contrast, many small equiaxed grains are isotopically distributed in the HAZ of low-carbon steel. These grains closest to the fusion zone have the largest size, and the grain size is inversely proportional to the distance from the fusion zone. These simulation results clearly show the mechanism of the formation of curved columnar grains in welded metals. It should be also noted that the grain orientations in the fusion zone are strongly influenced by the surrounding grain orientation and that the moving speed of the heat source can affect grain structures.

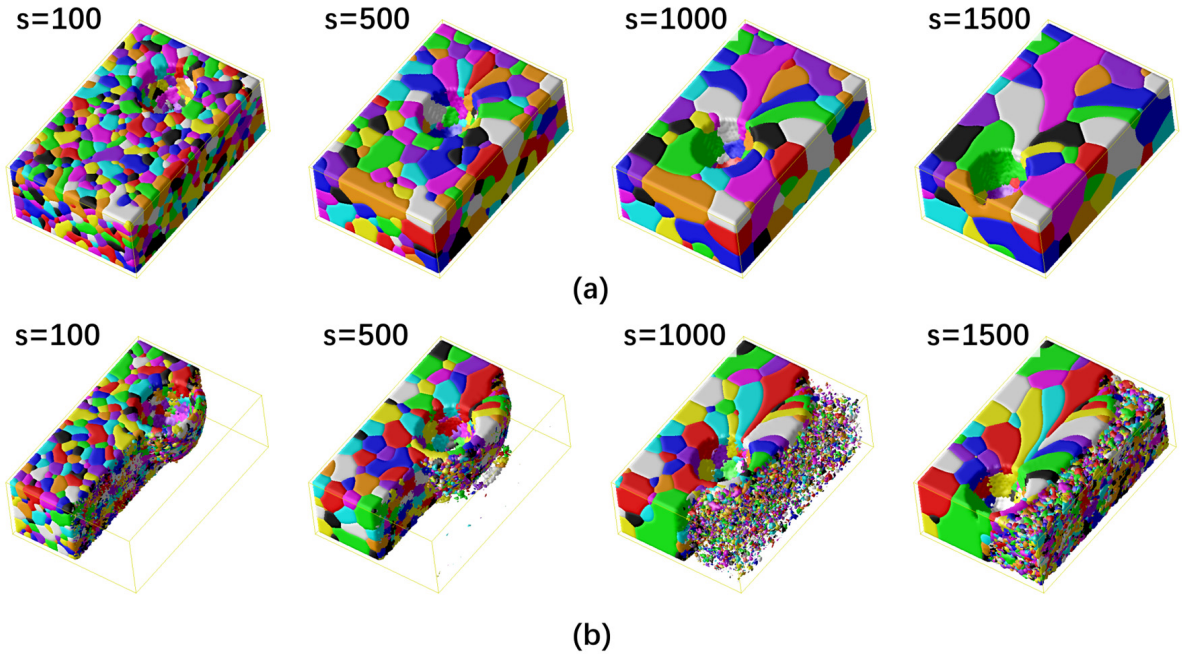

Figure 7. Temporal evolution of the grain structures during the welding of (**a**) two Fe–6.5 wt.% Si alloys and (**b**) Fe–6.5 wt.% Si alloy and low-carbon steel after different simulation steps. The different colors in the simulated grain structure represent the different orientations of the grains.

To verify the validity of numerical simulation results of the grain structures in the fusion zone and the HAZ during the welding process, experimental grain pictures and phase field results along the cross-sectional plane are illustrated in Figure 8. The details of the experimental setup can be found in Appendix A. The black dashed line in the simulation is the fusion line separating the fusion zone and the HAZ. Figure 8a shows the final grain structure during the welding process of joining low-carbon steel to Fe–Si alloy. The grains in the HAZ close to the fusion line grow into elongated columnar shapes. In contrast, grains that form farther away from the fusion line are usually small and equiaxed in the low-carbon steel site. It could be observed that the average grain size in the fusion zone is significantly smaller than that in the HAZ of Fe–Si alloy. This is because the kinetic undercooling during solidification makes grains in the melted fusion zone grow into equiaxed grains. There is good consistency between the experimental results and simulated grain structures.

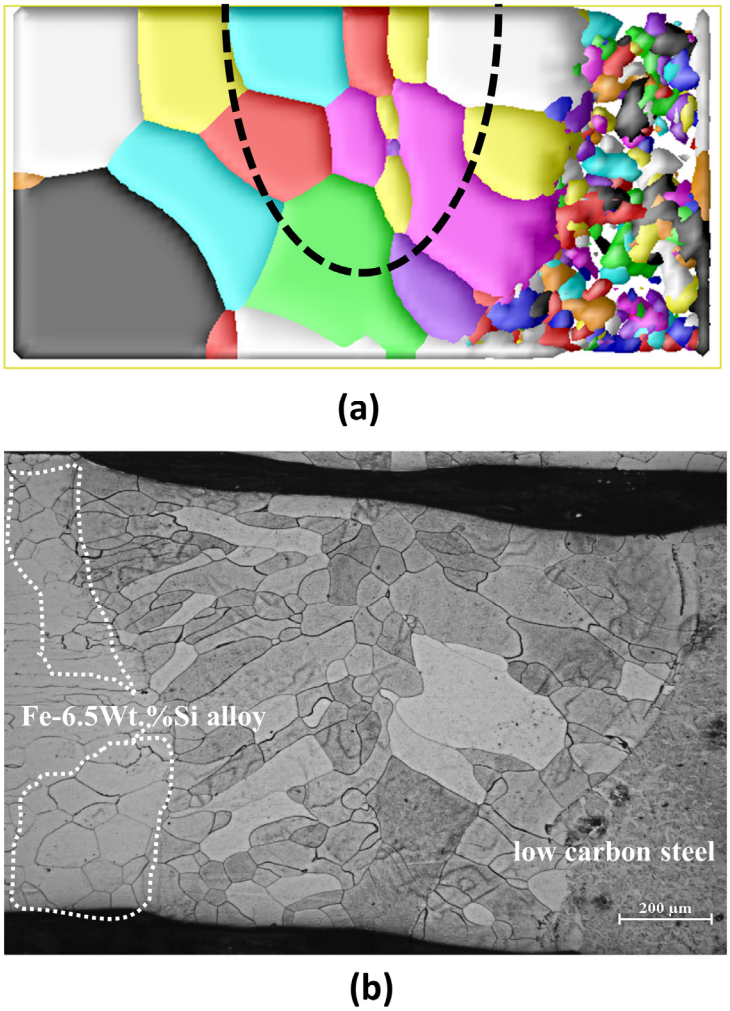

Figure 8. Comparison of (**a**) the simulated final grain structure and (**b**) the experimental results during the welding process of joining Fe–Si alloy and low-carbon steel. The different colors in the simulated grain structure represent the different orientations of the grains.

4. Conclusions

This paper developed a Monte-Carlo-assisted phase field model to simulate the grain growth process and grain structure evolution during welding. This work demonstrated the application of this model to several material processes, including the isothermal grain growth process, the continuous heat treatment process, and the welding process. Through a comparison of simulated structure and experimental observations, the following are the main conclusions:

(1) The experimentally determined average grain size agreed well with the corresponding simulation for all isothermal heat treatments. The rate of grain boundary migration is proportional to the temperature and inversely proportional to the average grain size. The rate of grain growth is faster during the initial stage and at high temperatures.

(2) The Monte-Carlo-assisted phase field model can be used to simulate grain growth in continuous heating treatment and is comparable with experimental results. It should be pointed out that the simulation accuracy is strongly dependent on the initial input grain structure.

(3) Three-dimensional simulations are required for a realistic welding process, and the grain size in the HAZ increases with time and is inversely proportional to the distance from the heat source. The grain growth rate in Fe–Si alloy is obviously larger than that in low-carbon steel. When joining low-carbon steel and Fe–6.5 wt.% Si alloy together using fusion welding, columnar grains are observed in the HAZ and equiaxed grains are formed

farther away from the fusion line. The average grain size in the fusion zone is significantly smaller than that in the HAZ of Fe–Si alloy. The simulated grain structures agreed well with the experimental results.

Works in progress include the construction of a model integrated with elastic energy based on Khachaturyan's theory of elasticity [41,42]. The advantage of the multi-phase field model is that the phase field order parameter η_i can be connected to the crystallographic orientation of the grain. In other words, all the grain orientations can be identified in our multi-phase field model; therefore, mechanical properties during/after heating or welding processes can be predicted. Such simulation is important not only for simulation works in the design or control of grain structures but also in the fundamental study of understanding how grain structures may affect the mechanical properties of metal/alloys after heating or welding treatment. This model also can be used to investigate grain evolutions in additive manufacturing processes.

Author Contributions: Conceptualization, Y.L., J.L. and P.W.; methodology, P.W.; validation, P.W.; investigation, Y.Z. and P.W.; data curation, Y.Z.; writing—original draft preparation, Y.Z.; writing—review and editing, J.L. and P.W.; visualization, Y.Z. and P.W.; supervision, P.W.; project administration, P.W.; funding acquisition, Y.L. and P.W. All authors have read and agreed to the published version of the manuscript.

Funding: This work was supported by the State Key Lab for Advanced Metals and Materials in the University of Science and Technology Beijing (contract no. 2021-ZD02) and the Cultivating Advanced Functional Materials Research Group Program of Xiamen Institute of Technology (contract no. KYTD202004). This work was also supported by the State Key Laboratory for Mechanical Behavior of Materials in the Xi'an Jiaotong University (contract no. 20212320).

Data Availability Statement: Not applicable.

Conflicts of Interest: The authors declare no conflict of interest.

Appendix A. Experimental Setup

In this study, the 1-mm-thickness-type Fe–6.5 wt.%Si alloy and low-carbon steel plate were welded in experiments, and the chemical compositions of the workpiece are listed in Table A1. The experiments used fiber laser welding equipment (PRC-3000). Different welding parameters (laser power and welding speed) were tested, and the final weld seams were obtained with a laser power of 1000 W and a welding speed of 1.0 m/min. Before welding, the joint of the plate to be welded was polished and alcohol and acetone were used to remove the oil on the surface of the specimens. After the welding experiment, the specimens were etched with the erosion agent 5% high-purity nitric acid. The cross-sectional micrographs of the weld were obtained with a ZEISS-SUPRA-55 field emission scanning electron microscope.

Table A1. The material compositions of Fe-6.5wt.%Si alloy and low-carbon steel.

Element	Chemical Content (wt.%)							
	C	Si	Mn	S	P	B	Al	Fe
Fe–6.5 wt.%Si alloy	0.022	6.3	0.031	0.0047	0.012	0.061	<0.005 (0.0048)	Bal.
Low-carbon steel (Q195)	0.07	0.15	0.2	0.02	0.11	——	——	Bal.

References

1. Brandt, M. *Laser Additive Manufacturing—Materials, Design, Technologies and Applications*; Woodhead Publishing: Duxford, UK, 2016.
2. Zaza, D.; Ciavarella, M.; Zurlo, G. Strain incompatibility as a source of residual stress in welding and additive manufacturing. *Eur. J. Mech.-A/Solids* **2021**, *85*, 104147. [CrossRef]
3. Wu, T.; Tinkloh, S.; Tröster, T.; Zinn, W.; Niendorf, T. Measurement and Analysis of Residual Stresses and Warpage in Fiber Reinforced Plastic and Hybrid Components. *Metals* **2021**, *11*, 335. [CrossRef]

4. Chen, L.Q.; Yang, W. Computer simulation of the domain dynamics of a quenched system with a large number of nonconserved order parameters: The grain-growth kinetics. *Phys. Rev. B Condens. Matter* **1994**, *50*, 15752–15756. [CrossRef] [PubMed]
5. Fan, D.; Chen, L.Q. Computer simulation of grain growth using a continuum field model. *Acta Mater.* **1997**, *45*, 611–622. [CrossRef]
6. Krill, C.E., III; Chen, L.Q. Computer simulation of 3-D grain growth using a phase-field model. *Acta Mater.* **2002**, *50*, 3059–3075. [CrossRef]
7. Asta, M.; Beckermann, C.; Karma, A.; Kurz, W.; Napolitano, R.; Plapp, M.; Purdy, G.; Rappaz, M.; Trivedi, R. Solidification microstructures and solid-state parallels: Recent developments, future directions. *Acta Mater.* **2009**, *57*, 941–971. [CrossRef]
8. Wang, K.G.; Ding, X.; Chang, K.; Chen, L.Q. Phase-field simulation of phase coarsening at ultrahigh volume fractions. *J. Appl. Phys.* **2010**, *107*, 061801. [CrossRef]
9. Bhattacharyya, S.; Heo, T.W.; Chang, K.; Chen, L.-Q. A phase-field model of stress effect on grain boundary migration. *Model. Simul. Mater. Sci. Eng.* **2011**, *19*, 035002. [CrossRef]
10. Heo, T.W.; Bhattacharyya, S.; Chen, L.-Q. A phase-field model for elastically anisotropic polycrystalline binary solid solutions. *Philos. Mag.* **2013**, *93*, 1468–1489. [CrossRef]
11. Chen, L.; Chen, J.; Lebensohn, R.A.; Ji, Y.Z.; Heo, T.W.; Bhattacharyya, S.; Chang, K.; Mathaudhu, S.; Liu, Z.K.; Chen, L.Q. An integrated fast Fourier transform-based phase-field and crystal plasticity approach to model recrystallization of three dimensional polycrystals. *Comput. Methods Appl. Mech. Eng.* **2015**, *285*, 829–848. [CrossRef]
12. Du, L.; Yang, S.; Zhang, P.; Du, H. Pinning effect of different shape second-phase particles on grain growth in polycrystalline: Numerical and analytical investigations. *Compos. Interfaces* **2018**, *25*, 357–368. [CrossRef]
13. Li, N.; Zhang, L.; Zhang, R.; Yin, P.; Wu, H.; Song, K.; Xing, H. The Role of Electric Current-Associated Free Energy and Forced Convection on Grain Refinement in Pure Aluminum under Electropulsing. *Materials* **2019**, *12*, 3846. [CrossRef]
14. Xing, H.; Ji, M.; Dong, X.; Wang, Y.; Zhang, L.; Li, S. Growth competition between columnar dendrite and degenerate seaweed during directional solidification of alloys: Insights from multi-phase field simulations. *Mater. Des.* **2020**, *185*, 108250. [CrossRef]
15. Liu, P.W.; Ji, Y.Z.; Wang, Z.; Qiu, C.L.; Antonysamy, A.A.; Chen, L.Q.; Cui, X.Y.; Chen, L. Investigation on evolution mechanisms of site-specific grain structures during metal additive manufacturing. *J. Mater. Process. Technol.* **2018**, *257*, 191–202. [CrossRef]
16. Fallah, V.; Amoorezaei, M.; Provatas, N.; Corbin, S.F.; Khajepour, A. Phase-field simulation of solidification morphology in laser powder deposition of Ti–Nb alloys. *Acta Mater.* **2012**, *60*, 1633–1646. [CrossRef]
17. Prosgolitis, C.G.; Lambrakos, S.G.; Zervaki, A.D. Phase-Field Modeling of Nugget Zone for a AZ31-Mg-Alloy Friction Stir Weld. *J. Mater. Eng. Perform.* **2018**, *27*, 5102–5113. [CrossRef]
18. Yang, C.; Wu, C.; Shi, L. Phase-field modelling of dynamic recrystallization process during friction stir welding of aluminium alloys. *Sci. Technol. Weld. Join.* **2019**, *25*, 345–358. [CrossRef]
19. Zheng, W.J.; Dong, Z.B.; Wei, Y.H.; Song, K.J.; Guo, J.L.; Wang, Y. Phase field investigation of dendrite growth in the welding pool of aluminum alloy 2A14 under transient conditions. *Comput. Mater. Sci.* **2014**, *82*, 525–530. [CrossRef]
20. Wang, L.; Wei, Y.; Zhan, X.; Yu, F. A phase field investigation of dendrite morphology and solute distributions under transient conditions in an Al–Cu welding molten pool. *Sci. Technol. Weld. Join.* **2016**, *21*, 446–451. [CrossRef]
21. Yu, F.; Wei, Y.; Ji, Y.; Chen, L.-Q. Phase field modeling of solidification microstructure evolution during welding. *J. Mater. Process. Technol.* **2018**, *255*, 285–293. [CrossRef]
22. Yang, C.; Wu, C.; Gao, S. Modified constitutive equation by using phase field simulation of dynamic recrystallization in friction stir welding. *J. Mater. Res. Technol.* **2021**, *12*, 916–929. [CrossRef]
23. Ali, B.; Heider, Y.; Markert, B. Residual stresses in gas tungsten arc welding: A novel phase-field thermo-elastoplasticity modeling and parameter treatment framework. *Comput. Mech.* **2021**, *69*, 565–587. [CrossRef]
24. Yang, M.; Wang, L.; Yan, W. Phase-field modeling of grain evolutions in additive manufacturing from nucleation, growth, to coarsening. *NPJ Comput. Mater.* **2021**, *7*, 56. [CrossRef]
25. Radhakrishnan, B.; Zacharia, T. Monte Carlo simulation of grain boundary pinning in the weld heat-affected zone. *Metall. Mater. Trans. A* **1995**, *26*, 2123–2130. [CrossRef]
26. Gao, J.; Thompson, R.G. Real time-temperature models for Monte Carlo simulations of normal grain growth. *Acta Mater.* **1996**, *44*, 4565–4570. [CrossRef]
27. Sista, S.; Yang, Z.; Debroy, T. Three-dimensional monte carlo simulation of grain growth in the heat-affected zone of a 2.25Cr-1Mo steel weld. *Metall. Mater. Trans. B* **2000**, *31*, 529–536. [CrossRef]
28. Sista, S.; Debroy, T. Three-dimensional monte carlo simulation of grain growth in zone-refined iron. *Metall. Mater. Trans. B* **2001**, *32*, 1195–1201. [CrossRef]
29. Rodgers, T.M.; Madison, J.D.; Tikare, V.; Maguire, M.C. Predicting Mesoscale Microstructural Evolution in Electron Beam Welding. *JOM* **2016**, *68*, 1419–1426. [CrossRef]
30. Wei, H.L.; Elmer, J.W.; DebRoy, T. Origin of grain orientation during solidification of an aluminum alloy. *Acta Mater.* **2016**, *115*, 123–131. [CrossRef]
31. Wei, H.L.; Elmer, J.W.; DebRoy, T. Three-dimensional modeling of grain structure evolution during welding of an aluminum alloy. *Acta Mater.* **2017**, *126*, 413–425. [CrossRef]
32. Beck, P.A.; Kremer, J.C.; Demer, L.J. Grain growth in highpurity aluminum. *Phys. Rev.* **1947**, *71*, 555. [CrossRef]
33. Burke, J.E.; Turnbull, D.M. Recrystallization and Grain Growth. *Prog. Met. Phys.* **1952**, *3*, 220–292. [CrossRef]
34. Holmes, E.L.; Winegard, W.C. Grain growth in zone-refined tin. *Acta Metall.* **1959**, *7*, 411–414. [CrossRef]

35. Brun, M.Y.; Gordienko, A.I.; Elagina, L.A.; Ivashko, V.V. Application of rapid heating in forming and heat treatment of titanium alloys. *Met. Sci. Heat Treat.* **1991**, *33*, 937–943. [CrossRef]
36. Zhang, Z.; Chen, G.; Bei, H.; Li, F.; Ye, F.; Chen, G.L.; Liu, C.T. Directional recrystallization and microstructures of an Fe–6.5wt%Si alloy. *J. Mater. Res.* **2011**, *24*, 2654–2660. [CrossRef]
37. Liang, Y.; Wang, S.; Qi, J.; Ye, F.; Lin, J. Microstructure and properties of cost-effective Fe–6.5 wt% Si ribbons fabricated by melt-spinning. *Scr. Mater.* **2019**, *163*, 107–110. [CrossRef]
38. Ouyang, G.; Chen, X.; Liang, Y.; Macziewski, C.; Cui, J. Review of Fe-6.5 wt%Si high silicon steel—A promising soft magnetic material for sub-kHz application. *J. Magn. Magn. Mater.* **2019**, *481*, 234–250. [CrossRef]
39. Li, J.; Fei, Y. Experimental Constraints on Core Composition. *Treatise Geochem.* **2003**, *2*, 568.
40. Zhang, Z.W.; Chen, G.; Chen, G.L. Dynamics and mechanism of columnar grain growth of pure iron under directional annealing. *Acta Mater.* **2007**, *55*, 5988–5998. [CrossRef]
41. Khachaturyan, A.G. *Theory of Structural Transformations in Solids*; John Wiley & Sons Inc.: New York, NY, USA, 1983.
42. Wu, P.; Liang, Y. Lattice Phase Field Model for Nanomaterials. *Materials* **2021**, *14*, 7317. [CrossRef] [PubMed]